Investigating the effect of sulphurization on volatility of compositions in Cu-poor and Sn-rich CZTS thin films

Journal Pre-proofs

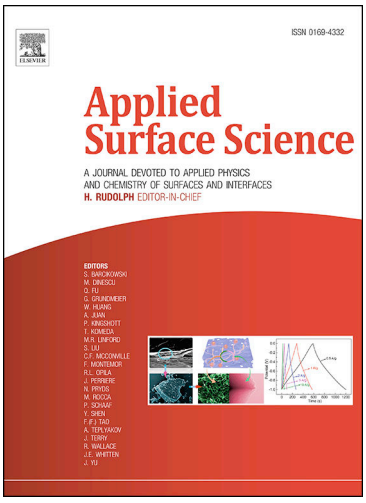

Full Length Article

Investigating the effect of sulphurization on volatility of compositions in Cu-poor and Sn-rich CZTS thin films

Manoj Vishwakarma, Khushboo Agrawal, B.R. Mehta

PII: S0169-4332(19)33860-7
DOI: https://doi.org/10.1016/j.apsusc.2019.145043
Reference: APSUSC 145043

To appear in: *Applied Surface Science*

Received Date: 11 September 2019
Revised Date: 26 November 2019
Accepted Date: 10 December 2019

Please cite this article as: M. Vishwakarma, K. Agrawal, B.R. Mehta, Investigating the effect of sulphurization on volatility of compositions in Cu-poor and Sn-rich CZTS thin films, *Applied Surface Science* (2019), doi: https://doi.org/10.1016/j.apsusc.2019.145043

Investigating the effect of sulphurization on volatility of compositions in Cu-poor and Sn-rich CZTS thin films

Manoj Vishwakarma[1], Khushboo Agrawal[1], B.R. Mehta[1*]

[1] Thin Film Laboratory, Department of Physics, IIT Delhi, New Delhi-110016, India

Abstract

In the present work, the Cu-poor and Sn-rich CZTS thin films were prepared in order to study the volatility of Sn with respect to other components. Thin film composition were kept intentionally Sn-rich to understand the behaviour of loss and segregation of Sn during sulphurization. The homogeneous composition distribution in precursor thin film turns into heterogeneous with change in morphology after sulphurization. The inability of identifying nanoscale secondary phases in CZTS thin film by conventional analytical techniques such as XRD and Raman, can be fulfilled by employing HAADF-STEM analysis. XPS and HAADF-STEM analysis provides the quantification of nanoscale secondary phases across the thin film and surface, respectively. The volatility of Sn was revealed in the form of segregation in the middle layer of CZTS cross-sectional lamella rather than loss to annealing atmosphere. It was observed that among the cations of CZTS, Sn segregates more than Cu, while Zn segregates least. The nanoscale spurious phases were observed to vary across different regions in the sulphurized CZTS sample. The reactive annealing lead to grain growth and formation of grain boundaries features in CZTS thin film, where annealing significantly modifies the potential difference and band bending at grain boundaries with respect to intra-grains.

Keywords: CZTS, off-stoichiometry, Kesterite phase, secondary phases, HAADF-STEM, XPS.

1. Introduction

Cu_2ZnSnS_4 (CZTS) based thin film with suitable optoelectronic properties ($\alpha \geq 10^4$ cm^{-1} and E_g ~1.4-1.5 eV) are considered to be a potential absorber for photovoltaic applications [1]. CZTS is a suitable alternative material to CIGS because of earth abundant and non-toxic constituent [1]. Various physical and chemical techniques have extensively been used for the synthesis of kesterite-type films. B. Shin et.al. have prepared the CZTS thin film by thermal evaporation and observed solar cell efficiency ~ 8.4 % [2]. In comparison, a CZTSSe thin film solar cell was prepared by pure hydrazine solution method achieved highest efficiency of 12.6 % [3]. However, further improvement in the efficiency of kesterite solar cells is limited by high open circuit voltage deficit, $^{E_g}/_{q} - V_{OC} \geq 0.6\, Volts$, where V_{oc} is the highest open circuit voltage reported in the CZTSSe solar cells [3]. There are a number of interdependent factors responsible for lower V_{OC} in the kesterite solar cells in comparison to the CIGS system [4]. Predominantly, the increase in photovoltaic efficiency is hindered due to the complex phase diagram of the CZTS [5]. Synthesizing defect free, single kesterite phase appears to be challenging because the stability of this quaternary compound is limited to a very narrow region in between the secondary phases $Cu_{2-x}S$, ZnS, SnS, SnS_2, Sn_2S_3 and Cu_2SnS_3 in the phase diagram [5]. Another important issue in obtaining homogenous Cu_2ZnSnS_4 thin films with stoichiometric composition ratio, Cu/(Zn+Sn)~0.8, Zn/Sn~1.2, is the loss of Sn due to the high volatility of SnS above 400^{o}C [6-8]. In order to maintain the stoichiometry of CZTS thin film, slightly higher Sn concentration is desirable to compensate the loss of SnS in precursor Cu-Zn-Sn-S thin film during sulphurization [9]. However, an excess amount of Sn may again lead to the presence of secondary phases in the CZTS thin film because of close relationship in between the compositional ratio and surface secondary phases [10]. Minor deviations from the stoichiometry can also lead to parallel growth of secondary phases in the kesterite system [11]. In the sulphide system (CZTS), three secondary phases Cu_xS, Cu_2SnS_3, SnS having a lower band gap than CZTS are supposed to co-exist, which are highly detrimental to the photovoltaic performance [12]. The presence of such phases in the surface region of CZTS thin film results in narrowing the band gap at the junction of CZTS/CdS solar cell devices [13]. Controlling the composition allows to leverage the density of defects present in the band gap of the photoactive material [14]. CZTS may also react with the Mo contact [15] generating Cu_2S, ZnS, SnS and MoS_2 during sulphurization process, which can promote the

formation of SnS_2 via condensation of Sn during the cooling process [16-17]. SnS_2 secondary phase has a large band gap (~2.24 eV) and its presence in CZTS will form a secondary diode as CZTS-SnS_2. CZTS-SnS_2 band alignment may induce a hole blocking layer for charge injection into the Mo-electrode, which will reduce the V_{oc} [18-19]. Hence, the CZTS-SnS_2 interface results in quenching the Fill factor because of higher series resistance and shunt conductance in the CZTS solar cell device [18]. Moreover, Sn-rich compositions in Cu-Zn-Sn-S system can result in growth of SnS and its presence on the surface will form an unfavorable band alignment with CdS unlike the CZTS. A SnS/CdS interface on the top surface of the CZTS layer could provide strong recombination centers in the CZTS/CdS solar cell device [20]. In the electrode deposition method, the Cu-content decreased with the decrease in potential while the Zn and S contents increased, however, the Sn content fluctuates with the change in the deposition potential during deposition [21]. In order to make control over the volatility of compositions, an investigation of the CZTS thin films before and after annealing process still need to be carried out at nanoscale level [21-22]. To investigate the volatility of composition, the off-stoichiometric Cu-poor and Sn-rich CZTS thin film samples were prepared on Mo-coated soda lime glass substrates. Phase analysis of the CZTS thin films were carried out by XRD, micro-Raman spectroscopy, transmission electron microscopic (TEM), X-ray photoelectron spectroscopy (XPS) and Kelvin probe force microscopy (KPFM) techniques, before and after sulphurization process.

2. Experimental

Cu_2ZnSnS_4 (CZTS) thin film samples were prepared on Mo-coated glass substrate by co-sputtering method using precursor targets of Cu, ZnS and SnS followed by a sulphurization step. The metal-alloy precursor thin films were deposited at room temperature for 60 minutes duration to achieve a thickness ~850 nm. Sulphurization is carried out using rapid thermal annealing (RTA) furnace for 20 minutes at 520°C with 120 mg sulphur powder in a closed graphite crucible and allowed to cool off to 350^{o}C over 15 minutes, subsequently decreasing to 120°C in 10 minutes and then left to cool down naturally. The above multistep temperature cooling is employed to reduce the pin-holes in the sulphurized CZTS thin film. Employing this synthesis method, two types of samples were prepared as, precursor thin film (S_RT) and sulphurized thin film (S_AN). In order to study the effect of sulphurization on precursor thin film, samples (S_RT) and (S_AN) were characterized. The macroscopic structural characterizations were carried out by using X-ray

diffraction (XRD) (Philips X'pert PRO-PW, Cu K_α) and micro-Raman spectroscopy (Renishaw invia confocal Raman microscope, laser~532 and 633 nm). Calibration for Raman measurement was performed using the Si main mode at 520 cm^{-1}. The nanoscale detailed structural and compositional analysis were performed by cross-sectional TEM analysis, using electron diffraction (ED), high angle annular dark field-scanning transmission electron microscopy (HAADF-STEM), energy dispersive X-ray (EDX) mapping modes and XPS analysis. The specimen for TEM study was prepared by focused ion beam (FIB) technique on a Be support. The TEM study was performed at a FEI Tecnai Osiris microscope operated at 200kV equipped with a Super-X detector. Surface analysis was carried out using X-ray photoelectron spectroscopy (XPS, Omicron ESCA). Monochromatic Al K_α (1486.7 eV) X-ray source with a mean radius of 124 mm was used at 3×10^{-10} mbar pressure in the chamber. The binding energy correction was performed by using the standard reference peak of C1s core spectra at 284.6 eV [23]. The peak fitting has been performed by using the software 'XPSPEAK41' where deconvolution were carried out by fixing the FWHM of the each component of the core spectra doublet. A nanoscope IIIa (Veeco metrology group, USA) set up was used to perform Kelvin probe force microscopy (KPFM) measurements. The surface potential (SP) images of the samples S_RT and S_AN were recorded using Pt-Ir coated Si-tip. Prior to recording of data, the work function of the tip was calibrated by using highly ordered pyrolytic graphite (HOPG) sample with a known value of workfunction (~4.8 eV). The work function of the KPFM tip was found to be ~4.81 eV.

3. Results and Discussion

The effect of sulphurization in Cu-poor and Sn-rich CZTS thin film samples was studied to understand its impact on composition distribution, growth of secondary phases and variations in structural and electronic properties. The X-ray diffraction pattern of sample S_RT shows amorphous nature, however, the annealed CZTS thin film S_AN has majority kesterite (JCPDS no. 26-0575) along with minority SnO_2 (JCPDS no. 41-1445) and SnS_2 (JCPDS 23-0677) secondary phases (Fig. 1) [24]. Since the thin film is grown on Mo-coated glass substrate, X-ray diffraction peaks corresponding to Mo (PDF no. 42-1120) were also observed [25]. Micro-Raman analysis was carried out to detect crystalline as well as amorphous phases in the samples. Raman spectra performed at 532 nm excitation source shows a broad peak at 337 cm^{-1} for sample S_RT, whereas, it indicates two peaks for sample S_AN at 337 cm^{-1} and 286 cm^{-1} attributing to kesterite

phase [Fig. 2(a)] [26]. It is worth noting that the use of different excitation wavelength allows to detect the secondary phases and additional modes related to kesterite phase [27]. Raman spectra at laser excitation source ~ 633 nm show a broad peak at 337 cm^{-1} for sample S_RT, whereas, sharp peaks were observed at 337 cm^{-1} and 370 cm^{-1} for S_AN [Fig. 2(b)]. The phase compositions of the thin film strongly depend on the precursors used for the growth of CZTS [28]. It is complicated to relate the stoichiometry of CZTS thin films with the co-existence of kesterite and secondary phases as determined using macroscopic techniques such as XRD and Raman spectroscopy. Therefore, nanoscale structural and compositional investigation were performed using TEM to determine the homogeneous distribution and segregation of phases across the cross-section of the absorber layer.

The cross-section lamella of the thin film [Fig. 3(a)] shows a total thickness of 1.3 µm for sample S_RT. It consists of an amorphous CZTS precursor layer L1 (thickness~ 850 nm) and a crystalline Mo layer (~450 nm). The precursor layer L1 is smooth and contains round slit like pores (dimension~ 5-7 nm) [Fig. 3(b)]. At the interface of layer L1 with Mo, there is a 5-7 nm thin layer with bright contrast [Fig. 3(c)], indicating the segregation of precursor particles. The diffraction patterns of the different layers of the cross-section of sample S_RT have been shown separately for the Pt layer, CZTS precursor layer L1, Mo layer and soda lime glass (Fig. 4). The ring diffraction pattern for layer L1 [Fig. 4(b)] shows only broad rings, indicating the amorphous nature of the layer which is in agreement with XRD and Raman analysis. As deposited CZTS thin film (layer 1) does not have the multilayer structure. Further, the BF-TEM image of sample S_AN revealed the multilayer structure of the CZTS thin film, where it comprises of top layer and middle layer [Fig. 5(a)]. The total thickness of the cross-section lamella of sample S_AN is ~ 1.5-1.6 µm, consisting of a top layer ~230-380 nm, middle layer ~ 740 nm, MoS_2 layer ~ 20-30 nm and Mo-layer ~ 470 nm. The top layer consists of CZTS crystallites of ~200 nm as shown in Fig. 5(b). The middle layer comprises of 0.1-1 µm crystallites, 7-15 nm crystalline nanoparticles [Fig. 5(c)]. In the ring diffraction pattern of the middle layer, bright reflections and continuous rings with low intensity, corresponding to the 0.1-1 µm crystallites are observed [Fig. 5(d)]. The rings correspond to the multitude of nanoparticles, and the position of the rings indicates that they correspond to SnO_2. In order to quantify the compositional distribution across the cross-section of the thin film, HAADF-STEM analysis are performed (Fig. 6-7). The composition ratio quantified from Fig. 6-7

are presented in the Table 1. The stoichiometric coefficient of Sn, $\boldsymbol{X_{Sn}} = \frac{\mathbf{4}[\boldsymbol{Sn}]}{([\boldsymbol{Cu}]+[\boldsymbol{Zn}]+[\boldsymbol{Sn}])}$ was also presented to co-relate the deviation of Sn relative to all metal components (Table 1) [29]. The EDX analysis shows that the sample S_RT is Cu-poor and Sn-rich in which Cu segregates near the Mo layer and is also present sporadically on the top surface of the layer L1 [green particle in Fig. 6 (b)]. Apparently, the Sn enriched stoichiometry at room temperature does not create a non-uniform distribution of compositions except insignificant segregation near the substrate and top surface. However, the as-deposited CZTS thin film turns into heterogeneous during sulphurization process (Fig. 7). The HAADF-STEM analysis shows that the distribution of cation (Cu, Zn, Sn) and anion (S) are not uniform in the sample S_AN (Fig. 7). Although the sulphurization was performed in the presence of Ar gas, the oxygen was found in the sample S_AN [Fig. 7(c)]. The average composition ratio for sample S_RT, Cu: Zn: Sn = 1.13: 0.64: 2.22 changed to Cu: Zn: Sn = 0.95: 0.77: 2.27 for sample S_AN due to reactive annealing (Table 1). It can be noticed that the average Cu-concentration decreases and Zn-concentration increases upon sulphurization process. No significant change was observed in Sn concentration for samples S_RT to S_AN (Table 1). Moreover, it was observed that the deviation in the average stoichiometry of the CZTS thin film is non-significant after sulphurization process. The only variation in the compositional ratio is prominent across the different layers and regions of sample S_AN (Table 1). The top layer and middle layer of sample S_AN contains higher Cu and Zn concentrations, respectively, as compared to the average composition ratio of the sample (Table 1). The Sn-concentration in sample S_AN is found to be present significantly higher in the middle layer in comparison to top layer (Table 1). Therefore, it can be inferred that Cu-moves towards the top of the surface while Sn segregate in the middle of the layer during sulphurization step. However, no such segregation was observed at the Mo/CZTS interface in sample S_AN [Fig. 7(b-c)]. Further, the compositional analysis was also performed in the different regions of the top layer of sample S_AN to study the phase formation and separations. The region-1 and region-4 in sample S_AN are near stoichiometric and contains CZTS phase. The complete absence of Zn content in region-2 of sample S_AN indicates presence of SnS and Cu_xS phases in that region. The region-3 is highly Cu-rich and shows significant presence of Cu_xS phase. The formation of the secondary phase Cu_xS at the top surface can be attributed to the volatile nature of Sn which is either due to evaporation of Sn or moving towards middle layer during sulphurization process [7-8]. Hence, the compositional ratio changes not only across the different layers but also within the different regions in a particular layer during the

sulphurization process. The segregation of SnO_2 and SnS phases in middle layer of sample S_AN results in a higher Sn concentration in the middle layer than the top layer. The appearance of O in the interior of the thin film can lead to diffusion of oxygen into grain boundaries [30]. The non-uniform distribution of the vacancies, substitutions and presence of spurious phases contribute to the total defect concentration across the absorber layer [31]. The TEM investigation shows that Sn concentration away from the stoichiometry of CZTS ($^{Cu}/_{Sn}$ ~1.7 and $^{Zn}/_{Sn}$ ~1.2) can affect the phase purity of the kesterite thin film. This can be attributed to the lack of sulphur vapour inside the cross-section lamella in comparison to the surface of the film during sulphurization process [32].

In order to study the top surface of the thin films, high-resolution X-ray photoelectron spectra (XPS) for elements Cu, Zn, Sn and S were recorded (Fig. 8). The XPS core spectra of constituent elements have observed shift in binding energies due to sulphurization of CZTS thin films have been presented in Table 2. The spin-orbit splitting energy (~ΔE) of the core spectra doublet have also been shown in the Table 2. The peak position of the $Cu2p_{3/2}$ state observed in sample S_RT decreases by binding energy~0.43 eV in sample S_AN attributing to the Cu^{+} chemical state (Table 2) [33]. Since the peak corresponding to Cu(II) state at binding energy ~934 eV was not observed, the surface of the sample S_AN missing CuS Secondary phase [33]. The peak position of the $Zn2p_{3/2}$ state in sample S_RT decreases by binding energy ~0.17 eV in sample S_AN attributing to Zn^{2+} state (Table 2) [33]. Similarly, $Sn3d_{5/2}$ state observed in sample S_RT decreases by 0.17 eV in sample S_AN attributing to the Sn^{4+} state (Table 2) [33]. However, the $S2p_{3/2}$ state observed at binding energy 161.28 eV was found at 161.27 eV in sample S_AN showing insignificant change ~0.01 eV (Table 2) [33]. The peak positions of $S2p_{3/2}$ state in samples S_RT and S_AN belongs to S^{2-} chemical state [33]. The difference between the binding energies of core level spectra of constituent's cation and anion in samples, S_RT and S_AN are very small because sample S_RT supposed to have amorphous CZTS phase as proved by Raman analysis (Fig. 2, 8). The core spectra of Sn observed one additional peak at ~496.97 eV and 496.71 eV in samples S_RT and S_AN, respectively which correspond to the Zn L3M45M45 Auger peak [Fig. 8 (c)] [34-35]. It can noticed that the spin-orbit splitting energies (~ΔE) of cations and anion did not found any significant change from sample S_RT to S_AN because the difference lies within the resolution limit of the instrument (Table 2). From the XPS analysis it has been confirmed that

the core level peaks of Cu, Zn, Sn lies at higher binding energy in comparison to their corresponding elemental form validating formation of a cation states [36].

The XPS analysis is also used to study the surface stoichiometry of the thin film samples by using the formula,

$$\text{Atomic \%} = \left\{\frac{A_x/S_x}{\sum_i A_i/S_i}\right\} \times 100\% \quad (1)$$

where, A, S are area under the peak and relative sensitivity factor, respectively [37]. Here, x represent the element name while i indicates the number of elements. The relative sensitivity factor along with the chemical shift and corresponding peak area were presented in the Table 2. The stoichiometry analysis of the sample S_RT and S_AN have been shown in the table 2, where stoichiometry analysis shows that the concentration of Cu, Sn decreases while it increases for Zn and S in sample S_AN than S_RT. The increase in Zn concentration in the XPS spectra of sample S_AN indicate that Zn migrates towards the top surface upon reactive annealing. The lower intensity in Sn3d spectra indicates the decrease in Sn-concentration on the top surface of sample S_AN in comparison to that of S_RT [Fig. 8(c)]. Due to the highly volatile properties of SnS at temperature over 400°C, Sn loss from the surface is inevitable and results in phase variation (e.g. secondary phases SnS, SnO_2) during reactive annealing of CZTS thin films [38]. The present observations regarding Sn segregation are contrary to the earlier observation of the Sn-loss to environment during sulphurization process of the precursor CZTS thin film [39]. Further, the increase in sulphur concentration in sample S_AN is due to adding more sulphur to the CZTS thin film during sulphurization process. In contrast to cations heterogeneous distribution across the thin film, S is observed to be homogeneous as proved by HAADF-STEM analysis. Therefore, the cross-sectional TEM measurements in the present case do not agree with the earlier claims of preparing the single kesterite phase proved by XRD and Raman measurements in the CZTS thin film. The effect of sulphurization process on volatility of composition and phase have been investigated in detailed, but its effect on grain growth and grain boundaries (G.B.) still need to be addressed. The presence and effects of spurious phases on G.B. can be explained with change in local electrical properties [40]. KPFM measurements provides the crucial information regarding the presence of nanoscale spurious phases because the local electrical properties of the top surface are supposed to be affected by the modification in composition ratio of kesterite thin film. KPFM measurements

are used to provide the surface potential (SP) map along with morphology map, as shown in Fig. 9(a-b, d-e). The morphology images of sample S_RT shows that the surface of CZTS thin film has segregated particles (sizes~ 200-500 nm) lying on precursor layer (highlighted by green rings) [Fig. 9(a)]. On the other hand, the annealed sample S_AN show big grains (sizes~ 500 nm- 1μm) and segregated feature was not observed [Fig. 9(d)]. The SP maps indicate drastically increase in the SP values of CZTS thin film after sulphurization step [Fig. 9(b, e)]. The morphology and SP map of sample S_AN shows the polycrystalline feature on the surface of CZTS thin film. In SP map of sample S_RT, the edges of particles show higher SP in comparison to the rest of regions, whereas SP map of sample S_AN shows higher SP at G.B. than grains [Fig. 9(b, e)]. Further, the workfunction of the sample is calculated by using the following relation,

$$\Phi_{Sample} = \Phi_{tip} + e.(S.P.) \qquad (2)$$

where e, S.P., Φ_{tip} and Φ_{sample} are the electron charge, surface potential, work function of tip and sample respectively [41]. In order to explain the variation of workfunction at grain and grain boundaries in the samples, roughness-workfunction profile has been presented in Fig. 9(c, f). In sample S_RT, the edge of particles indicate lower workfunction than the rest of region across the line profile and the difference of potential between the edge and particle is ≤ 30 mV [Fig. 9(c)]. But the GBs of the sample S_AN indicate higher workfunction than intra-grain region and the difference of potential between grains and G.B. is ≤ 110 mV [Fig. 9(f)]. Moreover, the higher workfunction on the G.B. in comparison to grain show upward band bending at G.B. in sample S_AN, whereas the particles boundaries in sample S_RT observed with downward band bending. Therefore, the sulphurization step not only inverts the band bending at G.B. with respect to grain but also increase potential difference. The band bending and higher potential difference at G.B. with respect to grain are considered to be benign character for faster carrier separation in the photovoltaic devices [42]. However, the presence of spurious phases and defects on surface can critically affects the electrical properties of grain boundaries of kesterite thin film which in turn will affect the band bending and band alignment with buffer layers in photovoltaic devices. The presence of secondary phases along with the kesterite phase will also fluctuate the band gap of the top surface because of multiphase structure which will act as recombination centres in CZTS/CdS based junction devices. It can be observed that the distribution of composition can very at nanoscale level because of sulphurization effects. The segregation of compositions are found to be

less dependent on stoichiometry but more on the reactive annealing conditions. Cu segregates in the top layer of the sample S_AN even though the compositions are Cu-poor attributed to sulphurization process. In contrast to earlier reported study, the present investigation revealed the segregation of Sn in the middle of the cross-section of the thin film instead of loss to environment. Moreover, the surface composition and phase distribution differs from the top layer of the thin film indicating the critical impact of reactive annealing in the kesterite material. Therefore, the effect of sulphurization on co-sputtered CZTS thin films was observed to be a crucial step for controlling secondary phase formation during the growth of kesterite thin film. The insignificant change in average stoichiometry revealed that the segregation of composition is dominants over than loss to annealing environment.

4. Conclusion

The macroscopic analytical tools such as, XRD and Raman spectroscopy are found to be unable to detect secondary phases. The presence of secondary phases can effectively be quantified by using HAADF-STEM mapping and XPS surface analysis. It can also be concluded that the loss of compositions in the CZTS thin film is less prominent than heterogeneous distribution and the later depends on reactive annealing conditions. Additionally, the growth of secondary phases at nanoscale level increases the defect density which will modify the grain boundaries of the kesterite layer negatively even though the majority of the material have kesterite phase. The sulphurization process is found to be a crucial step in preparing homogeneous kesterite thin film samples. Therefore, nanoscale growth of spurious phases can be suppressed by achieving control over stoichiometry and annealing conditions.

Acknowledgement

Authors acknowledges support provided by DST in the forms of InSOL project. We also acknowledge Prof. Joke Hadermann EMAT, University of Antwerp, Groenenborgerlaan 171, B-2020 Belgium for helping in TEM measurements and Dr. Indrani Mishra for XPS measurements. Manoj Vishwakarma acknowledges IIT Delhi for MHRD fellowship. Prof. B.R. Mehta acknowledges the support of the Schlumberger chair professorship. M.V. also acknowledges the DST-FIST Raman facility.

Reference:

1. C. Shi, G. Shi, Z. Chen, P. Yang, M. Yao, Mater. Lett. 73 (2012) 89–91.
2. B. Shin, O. Gunawan, Y. Zhu, N. A. Bojarczuk, S. J. Chey, S. Guha, Prog. Photovolt: Res. Appl. 21 (2013) 72-76.
3. W. Wang, M. T. Winkler, O. Gunawan , T. Gokmen , T. K. Todorov,Y. Zhu, D. B. Mitzi, Adv. Energy Mater. 4 (2014) 1301465
4. D. B. Mitzi, O. Gunawan, T. K. Todorov, D. A. R. Barkhouse, Philos. Trans. R. Soc. London, Ser. A 371 (2013) 20110432.
5. S. Chen, J. H. Yang, X. G. Gong, A. Walsh, S. H. Wei, Phy. Rev. B 81 (2010) 245204.
6. M. Kumar, A. Dubey, N. Adhikari, S. Venkatesanb Q. Qiao, Energy Environ. Sci. 8 (2015) 3134-3159.
7. A. Weber, R. Mainz, H. W. Schock, J. Appl. Phys. 107 (2010) 013516.
8. J. J. Scragg, T. Ericson, T. Kubart, M. Edoff, and C. P. Bjorkman, Chem. Mater. 23 (2011) 4625–4633.
9. G. Chen, W. Wang, J. Zhang, S. Chen, Z. Huanga, Mater. Lett. 186 (2017) 98–101.
10. O. V. Galán, M. Courel, M. E. Rodriguez, V. I. Roca, E. Saucedo, A. Fairbrother, Sol. Energy Mater. Sol. Cells 117 (2013) 246–250.
11. I. D. Olekseyuk, I. V. Dudchak, L. V. Piskach J. Alloys Compd. 368 (2004) 135–143.
12. S. Siebentritt, Thin Solid Films 535 (2013) 1–4.
13. A. Crovetto, M. L. N. Palsgaard, T. Gunst, T. Markussen, K. Stokbro, M. Brandbyge, O. Hansen, Appl. Phys. Lett. 110 (2017) 083903.
14. G. Larramona, S. Levcenko, S. Bourdais, A. Jacob, C. Chone, B. Delatouche, C. Moisan, J. Just ,T. Unold, G. Dennler, Adv. Energy Mater. 5 (2015) 1501404.
15. A. Redinger, D. M. Berg, P. J. Dale, S. Siebentritt, J. Am. Chem. Soc. 133 (2011) 3320–3323.
16. J. J. Scragg, J. T. Watjen, M. Edoff, T. Ericson, T. Kubart and P. B. Charlotte, J. Am. Chem. Soc. 134 (2012) 19330–19333.
17. J. J. Scragg, T. Kubart, J. T. Watjen, T. Ericson, K. L. Margareta, P. B. Charlotte, Chem. Mater. 25 (2013) 3162–3171.
18. K. F. Tai, O. Gunawan, M. Kuwahara, S. Chen, S. G. Mhaisalkar, C. H. A. Huan, D. B. Mitzi, Adv. Energy Mater. 6 (2016) 1501609.
19. W. Wang, G. Chen, H. Cai, B. Chen, L. Yao, M. Yang, S. Chen, Z. Huang, J. Mater. Chem. A 6 (2018) 2995–3004.
20. D. Lim, H. Suh, M. Suryawanshi, G. Y. Song, J. Y. Cho, J. H. Kim, J. H. Jang, C. W. Jeon, A. Cho, S. Ahn, J. Heo, Adv. Energy Mater. 8 (10) (2018) 1702605.
21. Aiy Tang, Zhilin Li, Feng Wang, Meiling Dou, Youya Pan, Jingyu Guan, Appl. Surf. Sci. 402 (2017) 70–77.
22. A. Santoni, F. Biccari, C. Malerba, M. Valentini, R. Chierchia, A. Mittiga, J. Phys. D: Appl. Phys. 46 (2013) 175101.
23. S. S. Surah, M. Vishwakarma, R. Kumar, R. Nain, S. Sirohi, G. Kumar, Results Phys. 12 (2019) 1725-1731.
24. R. S. Yu, T. C. Hung, Appl. Surf. Sci. 364 (2016) 909–916.

25. S. M. Pandharka, S. R. Rondiya1, A. V. Rokade, B. B. Gabhale, H. M. Pathan, S. R. Jadkar, Front. Mater. 5 (13) (2018) 1-6.
26. J. J. S. Scragg, L. Choubrac, A. Lafond, T. Ericson, C. P. Bjorkman, Appl. Phys. Lett. 104 (2014) 041911.
27. X. Fontane, V. I. Roca, E. Saucedo, S. Schorr, V. O. Yukhymchuk, M. Y. Valakh, A. P. Rodriguez, J. R. Morante, J. Alloys Compd. 539 (2012) 190–194.
28. Y. Guo, J. Wei, Y. Liu, T. Yang, Z. Xu, Nanoscale Res. Lett. 12 (2017) 181.
29. C. Malerba, F. Biccari, C. L. A. Ricardo, M. Valentini, R. Chierchia, M. Muller, A. Santoni, E. Esposito, P. Mangiapane, P. Scardi, A. Mittiga, J. Alloys Compd. 582 (2014) 528–534.
30. R. Haight, X. Shao, W. Wang, D. B. Mitzi, Appl. Phys. Lett. 104 (2014) 033902.
31. T. Gokemen, O. Gunawan, T. K. Todorov, D. B. Mitzi, Appl. Phys. Lett. 103 (2013) 103506.
32. C. Andres, S. G. Haass, Y. E. Romanyuk, and A. N. Tiwari, Thin Solid Films, 633 (2016) 141-145.
33. O. Stroyuk, A. Raevskaya, O. Selyshchev, V. Dzhagan, N. Gaponik, D. R. T. Zahn, A. Eychmuller, Sci. Rep. 8 (2018) 13677.
34. M. Danilson, M. Altosaar, M. Kauk, A. Katerski, J. Krustok, J. Raudoja, Thin Solid Films 519 (2011) 7407–7411.
35. Y. Ren, J. J. S. Scragg, M. Edoff, J. K. Larsen, C. P. Bjorkman, Appl. Mater. Interfaces 8 (28) (2016) 18600–18607.
36. S. Hufner, Photoelectron Spectroscopy, Springer, Berlin, 2003.
37. D. Briggs, M. P. Seah, Practical surface analysis; Auger and X-ray photoelectron spectroscopy, Wiley, 1990.
38. J. J. Scragg, T. Ericson, T. Kubart, M. Edoff, C. P. Bjorkman, Chem. Mater. 23, 4625–4633 (2011).
39. J. Zhong, Z. Xia, M. Luo, J. Zhao, J. Chen, L. Wang, X. S. Liu, D. J. Xue, Y. B. Cheng, H. S. Song, J. Tang, Sci. Rep. 4 (2014) 6288.
40. J. Kim, G. Y. Kim, W. Jo, K. J. Yang, J. H. Sim, D. H. Kim, J. K. Kang, RSC Adv. 6 (2016) 103337–103345.
41. W. Melitz, J. Shena, A. C. Kummel, S. Lee, Surf. Sci. Rep. 66 (2011) 1–27.
42. M. J. Romero, H. Du, G. Teeter, Y. Yan, M. M. Al-Jassim, Phy. Rev. B 84 (2011) 165324.

Figure Captions

Fig. 1 XRD pattern of CZTS thin film samples, S_RT and S_AN.

Fig. 2 Micro-Raman analysis of the CZTS thin film samples, S_RT and S_AN at different excitation laser sources; (a) 532 nm and (b) 633 nm.

Fig. 3 Sample S_RT: BF-TEM images of (a) the cross-section lamella, (b) Layer 1 (Arrow indicating slit like pores), (c) the Mo/Layer 1 interface.

Fig. 4 S_RT: The SAED ring diffraction patterns from (a) Pt, (b) Layer 1 (L1), (c) Mo and (d) soda-lime glass (SLG) regions.

Fig. 5 S_AN: (a) BF-TEM image of the cross-section lamella, (b) the top part of the thin film, (c) middle layer showing 7-15 nm crystalline particles overlapping the μm-size crystallites, (d) The SAED ring diffraction pattern of middle layers. It contains distinguishable rings, which correspond to SnO_2.

Fig. 6 S_RT: (a) HAADF-STEM image of cross-sectional lamella, (b) {Cu, Zn, Sn, Mo} mixed map, and (c) {S, O, Si, Mo, Pt} mixed map of CZTS thin film.

Fig. 7 S_AN: (a) HAADF-STEM image, (b) {Cu, Zn, Sn, Mo} mixed map, (c) {S, Mo, O, Si, Pt} mixed map.

Fig. 8 XPS spectra of elements Cu2p, Zn2p, Sn3d and S2p states of samples S_RT and S_AN.

Fig. 9 S_RT: (a) Morphology, (b) Surface potential map, and (c) Roughness-Workfunction profile. S_AN: (d) Morphology, (e) Surface potential map, and (f) Roughness-Workfunction profile.

List of Tables

Table. 1 Compositional analysis of the thin film samples S_RT and S_AN.

Elements	Compositional distribution in Sn-rich CZTS thin film samples							
	S_RT	S_AN						
	Average	Average	Top layer (I)	Middle layer (II)	Top layer (I)			
					Region-1	Region-2	Region-3	Region-4
Cu	1.13	0.95	1.52	0.64	2.12	0.35	3.8	2.07
Zn	0.64	0.77	0.73	0.90	1.16	0	0.58	1.16
Sn	2.22	2.27	1.75	2.85	1.08	3.12	0.52	1.05
S	N. A.	N. A.	4.0	3.6	3.63	4.52	3.1	3.71
X_{Sn}	2.23	2.27	1.75	2.59	0.99	3.59	0.42	0.98

Table. 2 The XPS peak position of composition and their atomic percentage analysis in the CZTS samples [33-37].

Element	Core level	RSF (S_X)	S_RT				S_AN			
			Peak position (eV)	ΔE (eV)	Peak area	Atomic %	Peak position (eV)	ΔE (eV)	Peak area	Atomic %
Cu	$2p_{3/2}$	4.2	932.7	19.87	15007.96	26.7	932.27	19.89	9707.28	16.0
Zn	$2p_{3/2}$	4.8	1021.4	23.11	3861.95	6.0	1021.23	23.06	7600.81	11.0
Sn	$3d_{5/2}$	4.3	486.1	8.42	14936.13	26.0	485.93	8.4	7842.12	12.7
S	$2p_{3/2}$	0.49	161.28	1.12	2712.85	41.4	161.27	1.12	4254.68	60.3

Graphical abstract

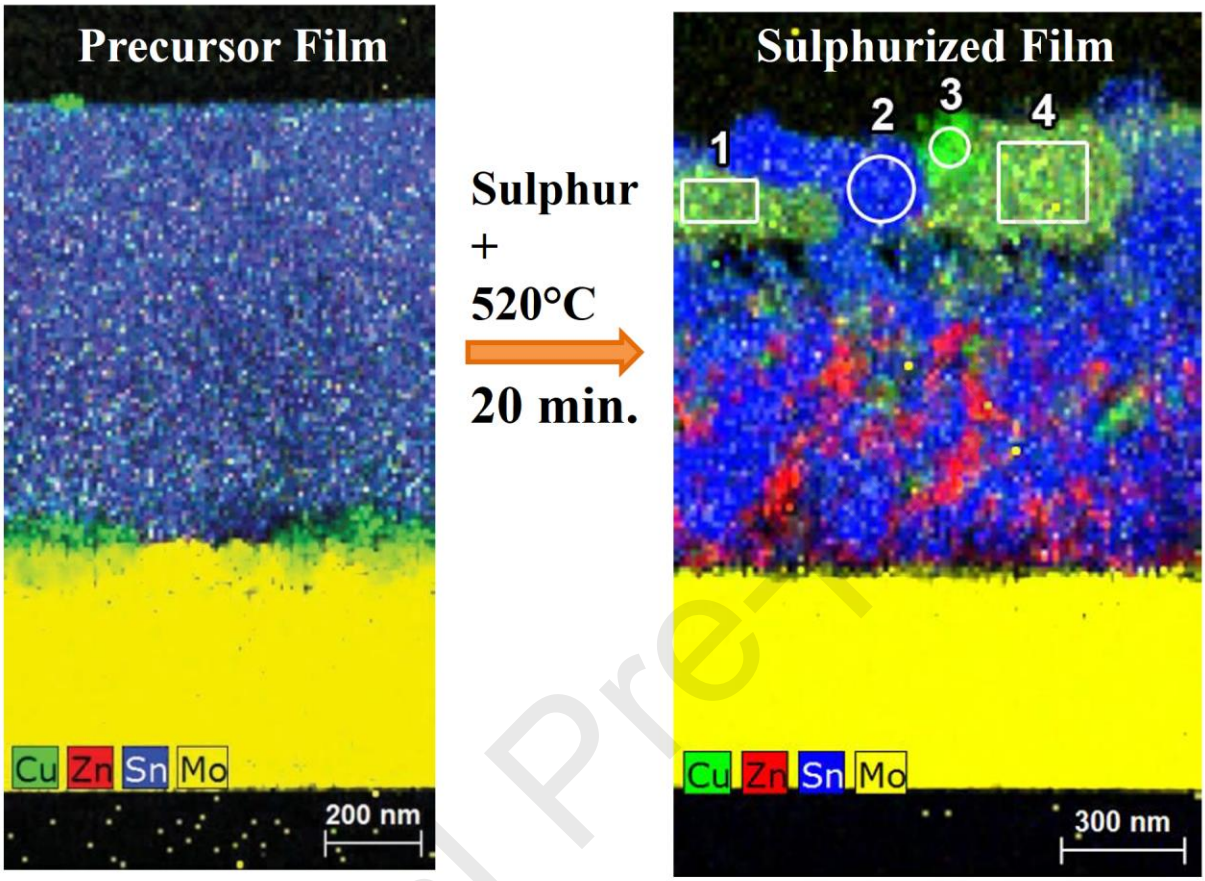

Highlights

1. The Cu-poor and Sn-rich composition ratio provides detailed information about the volatility of Sn across the CZTS thin film.
2. HAADF-STEM investigations revealed the heterogeneous distribution of the composition across the cross-sectional lamella of the CZTS thin film.
3. The sulphurization process drives grain growth and structural change in the CZTS thin film which lead to growth of kesterite phase along with secondary phases due to off-stoichiometric compositions.

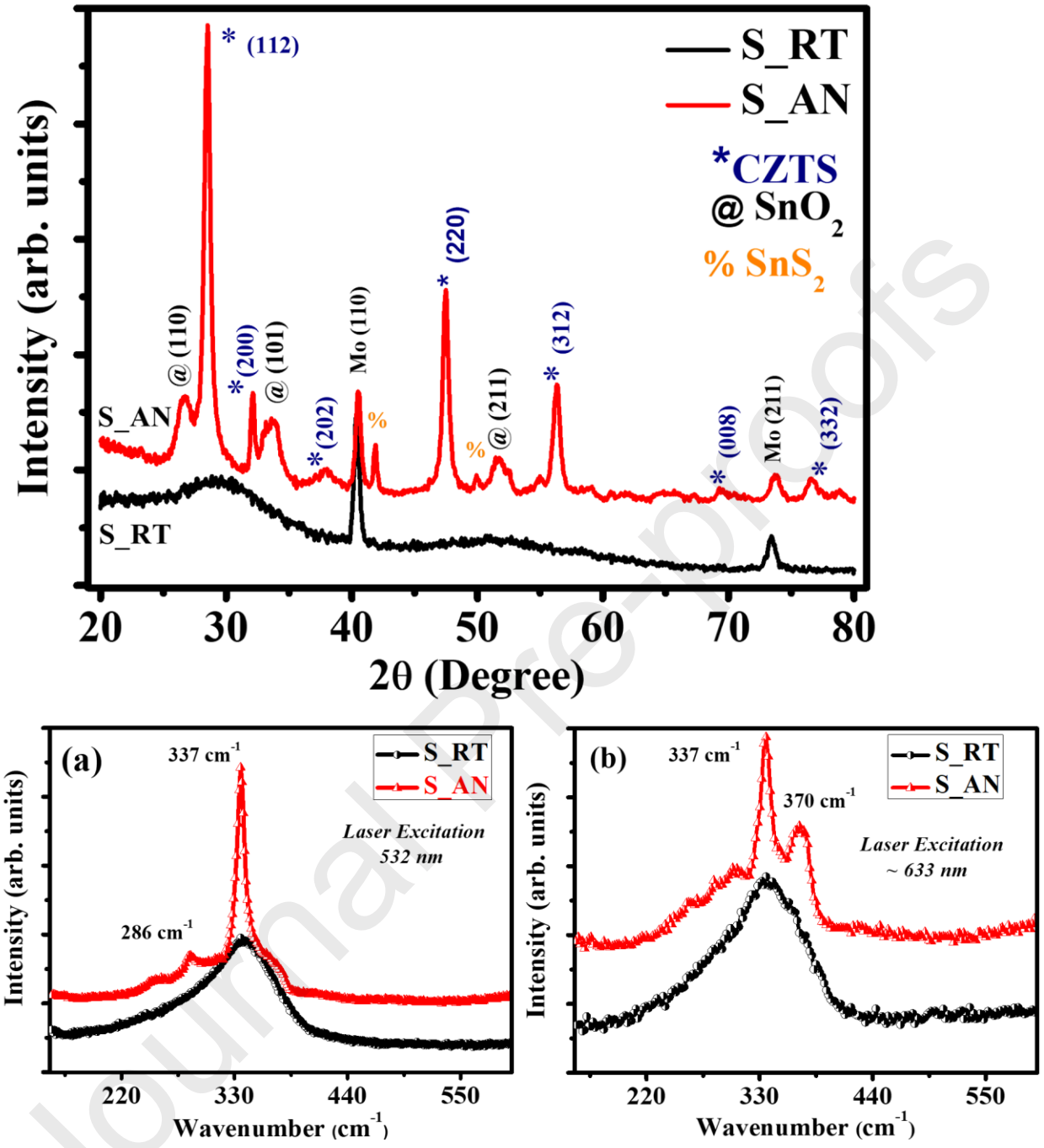

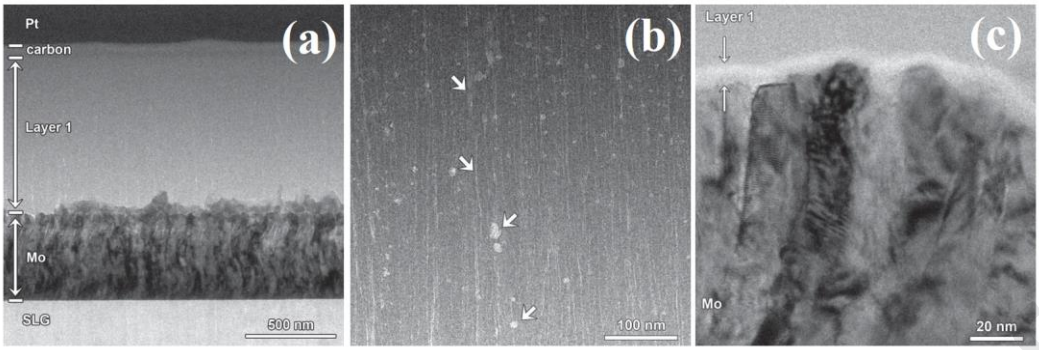

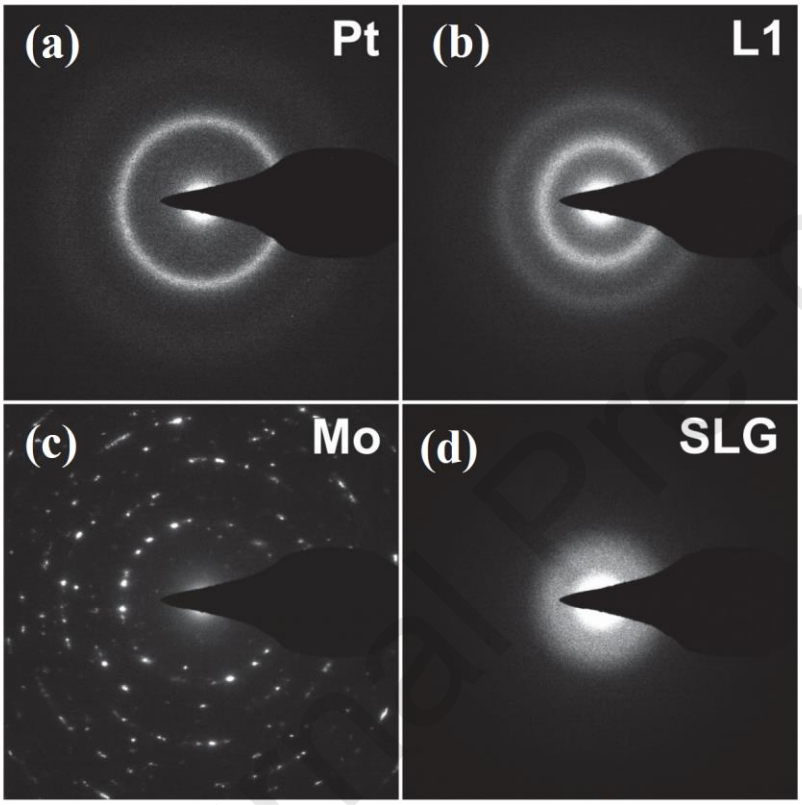

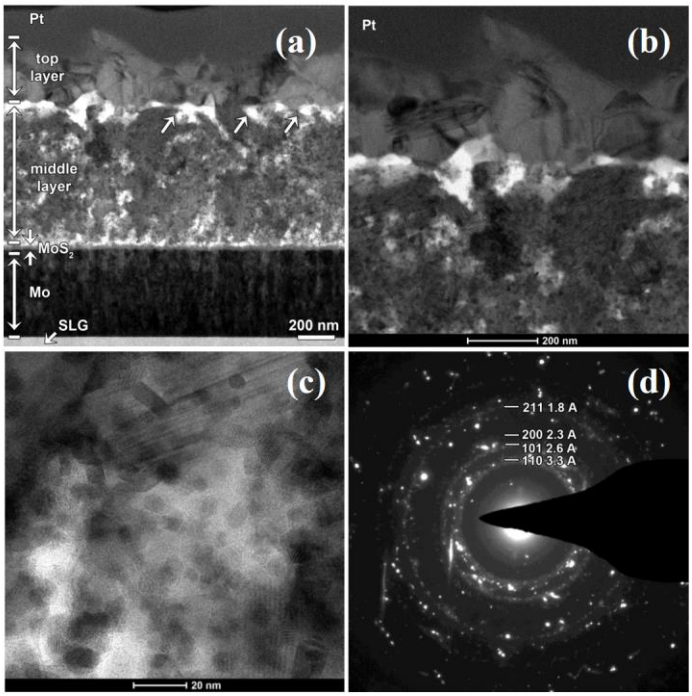
Pt
(a)
top layer
middle layer
MoS2
Mo
SLG
200 nm
Pt
(b)
200 nm
(c)
20 nm
(d)
211 1.8 A
200 2.3 A
101 2.6 A
110 3.3 A

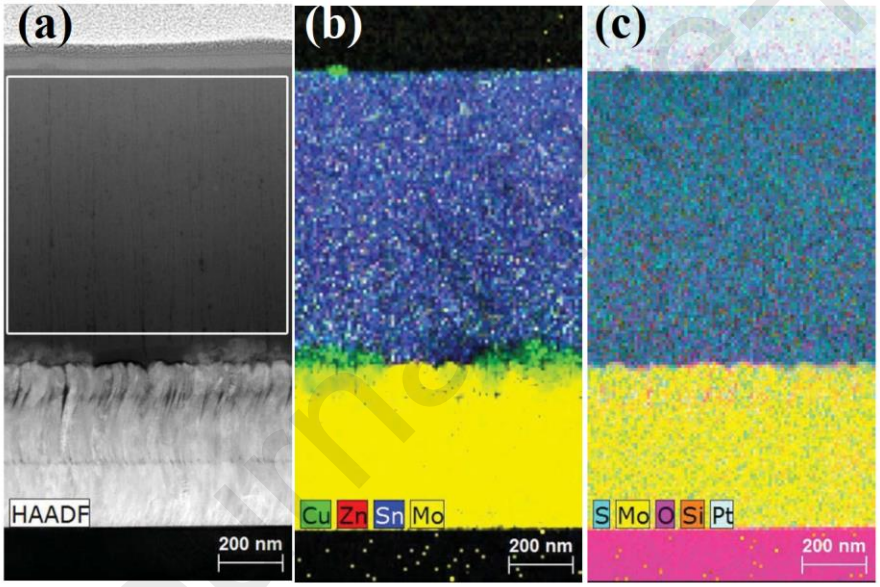
(a)
HAADF
200 nm
(b)
Cu Zn Sn Mo
200 nm
(c)
S Mo O Si Pt
200 nm

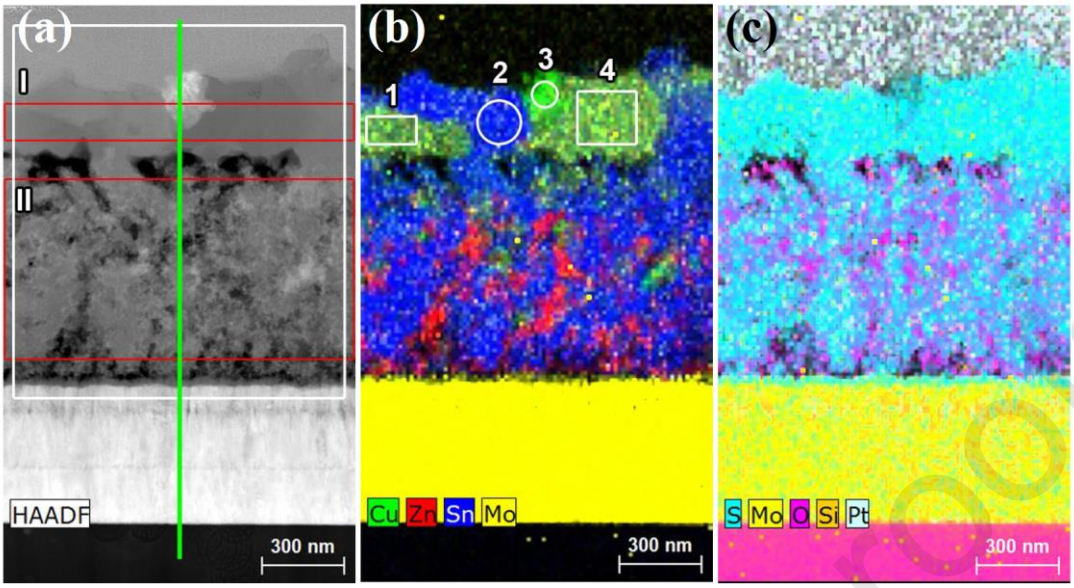

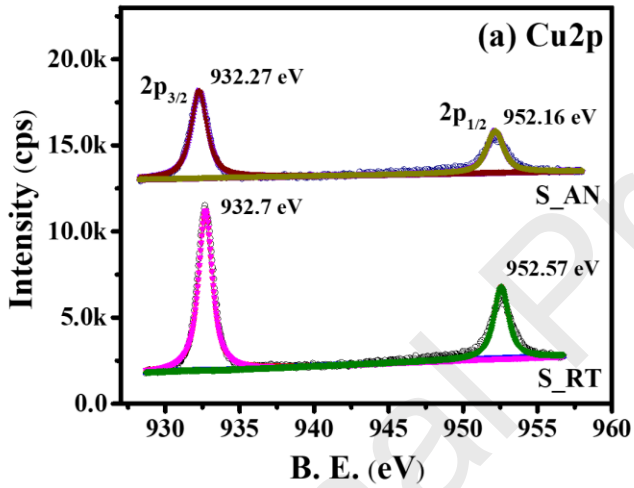

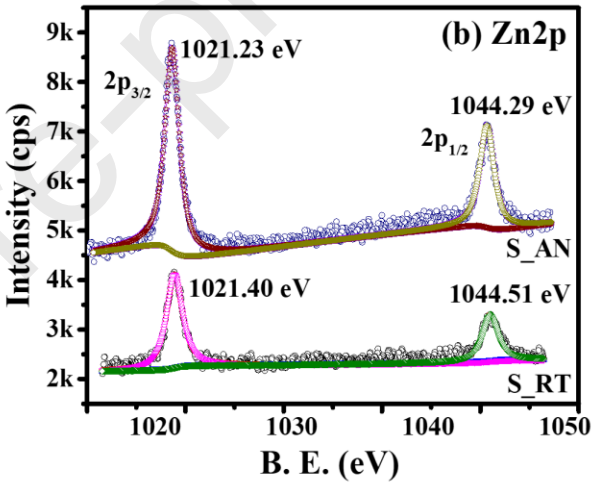

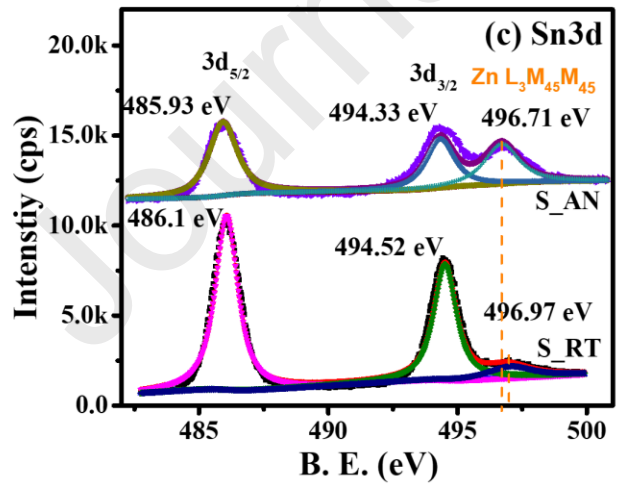

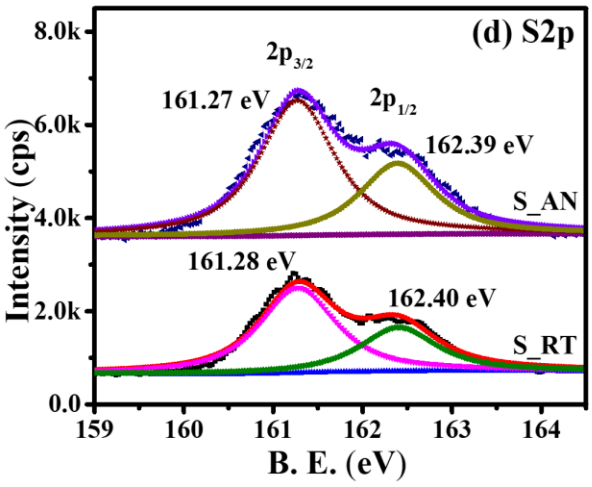

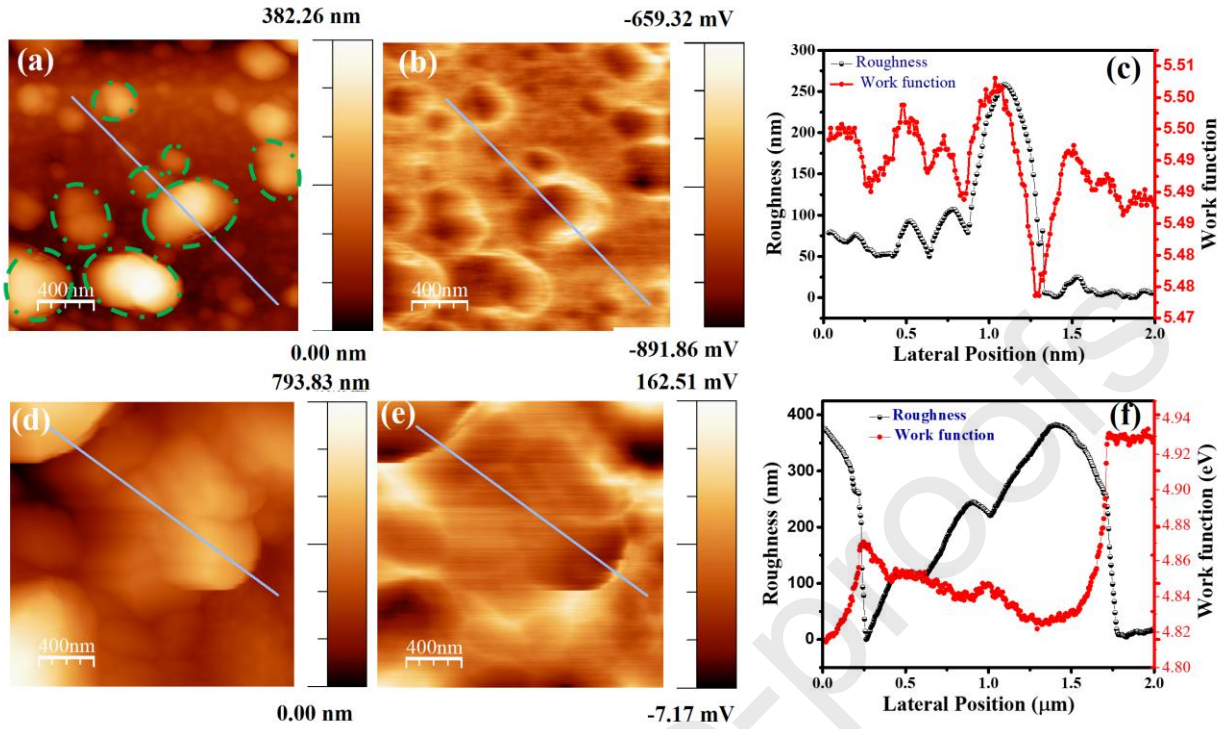

- The corresponding author is responsible for ensuring that the descriptions are accurate and agreed by all authors.
- Manoj Vishwakarma is responsible for Conceptualization, Methodology, Validation, Investigation, Writing - Original Draft and Visualization.
- B. R. Mehta and Khushboo Agrawal are responsible for supervision of this work.

Declaration of interests

☒ The authors declare that they have no known competing financial interests or personal relationships that could have appeared to influence the work reported in this paper.

☐The authors declare the following financial interests/personal relationships which may be considered as potential competing interests: